ADVANCED FUNCTIONAL MATERIALS
www.afm-journal.de

Flexible Mini-Inductors with Ultra-High Inductance Density Directly Cut from Soft Magnetic Amorphous Alloys by Femtosecond Laser

Yanan Chen, Yan Zhang, Ji Wang, Zhihao Chen, Xiaowen Cao, Fei Han, Bowen Zang, Mingliang Xiang, Juntao Huo, Wenwu Zhang,* and Jun-Qiang Wang**

Inductors are indispensable parts in power modules of electronic devices. With the rapid development of flexible and wearable electronic devices, developing flexible micro-inductors with large energy storage has become an urgent task. In this research, a sophisticated femtosecond laser ablation technique is employed to craft circular spiral mini-inductors via selective etching of soft magnetic amorphous alloy ribbons. Remarkably, while these inductors possess dimensions akin to human fingerprints, they demonstrate an impressively elevated inductance value of ≈1.15 µH at 1 MHz. The inductance density is ≈280–390 nH mm^{-2}, which is ≈10 times larger than conventional circular spiral inductors and is attributed to the high permeability of the amorphous alloys. Furthermore, the inductors showcase commendable flexibility, marked by stellar elasticity and a bending endurance exceeding 2500 cycles, thanks to the amorphous alloys' superior elastic strain limit. When integrated with an LM2576-3.3BT buck converter, the fabricated inductor achieved a peak power conversion efficiency nearing 70%. These findings underscore the potential of such flexible mini-inductors in the landscape of flexible electronics.

1. Introduction

The rapid development of high-performance, large-area microelectronics and flexible electronics with exceptional mechanical properties has become a focal point in contemporary research.[1,2] Unlike their traditional rigid counterparts, flexible electronics offer distinct advantages, including reduced weight, slim design, and superior flexibility and ductility. As a result, they present promising applications across a myriad of sectors, including information technology, energy, healthcare, and defense.[3–7] Yet, the progress in this domain often grapples with design challenges. One of the pivotal components impeding further miniaturization and flexibility is the inductor.[8,9]

The need for compact yet efficient power modules in various application scenarios drives the search for innovative solutions to enhance inductance density. Thin-film inductors with soft magnetic cores have gained prominence in this endeavor.[10-13] Most contemporary designs integrate these inductor coils onto flexible substrates, such as polyimides, aligning with the requirements of flexible applications.[14–17] However, there is an evident gap in material choice for these coils. Predominantly composed of Cu or Ag, these non-magnetic materials introduce significant magnetic leakage.[18,19] The magnetic leakage will reduce the inductance density, thereby reducing the inductor performance. This leakage curtails the inductance density, subsequently diminishing the inductor's overall performance. As a result, these inductors, restricted to a few nano-Henry (nH), are best suited for radio frequency (RF) applications and remain inadequate for high-demand scenarios like direct current-direct current (DC-DC) converters.[20–22]

Fe-based amorphous alloys have excellent properties, including soft magnetic properties and strong mechanical properties.[23,24] Their high permeability notably reduces magnetic leakage in contrast to non-magnetic material-based inductors. Additionally, their superior saturation magnetization implies an augmented electromagnetic energy storage capability. Complementing these magnetic properties, the elasticity of amorphous ribbons is ≈2%, surpassing that of crystalline materials, which is ≈0.5%. This heightened elasticity ensures commendable bending flexibility.[25] Collectively, these properties accentuate the feasibility of Fe-based amorphous alloys in the domain of flexible micro-inductors.[26–28]

Y. Chen, Y. Zhang, J. Wang, Z. Chen, X. Cao, F. Han, B. Zang, M. Xiang, J. Huo, W. Zhang, J.-Q. Wang
CAS Key Laboratory of Magnetic Materials and Devices, and Zhejiang Province Key Laboratory of Magnetic Materials and Application Technology
Ningbo Institute of Materials Technology and Engineering
Chinese Academy of Science
Ningbo 315201, China
E-mail: yzhang@nimte.ac.cn; zhangwenwu@nimte.ac.cn; jqwang@nimte.ac.cn
Y. Chen, Y. Zhang, J. Huo, W. Zhang, J.-Q. Wang
Center of Materials Science and Optoelectronics Engineering
University of Chinese Academy of Sciences
Beijing 100049, China

The ORCID identification number(s) for the author(s) of this article can be found under https://doi.org/10.1002/adfm.202313355

DOI: 10.1002/adfm.202313355

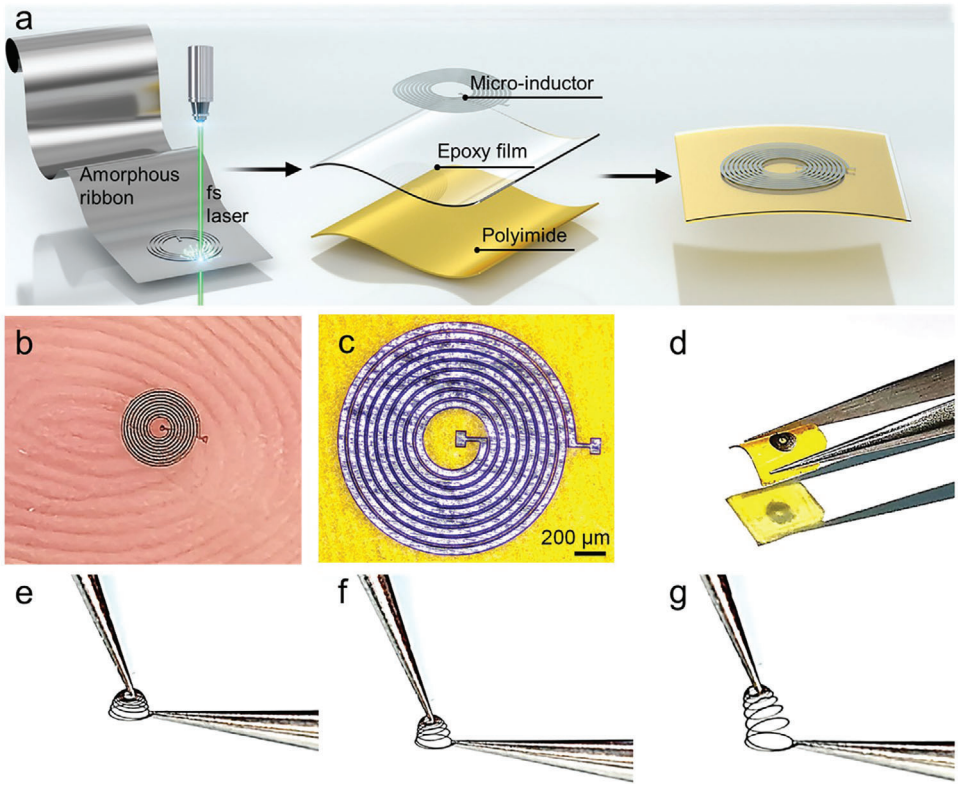

Figure 1. Design and characterization of the flexible inductor based on amorphous alloys. a) Schematic illustration for the design of flexible inductor using femtosecond laser. b) Optical image of a nine-turn flexible inductor on the finger. c) The zoomed-in optical image of the nine-turn flexible inductor. d) The micro inductor in the bending state. e–g) The inductor under different stretching deformations, the deformation increases gradually.

To harness the benefits of these alloys, our study deploys high-precision femtosecond laser ablation technology to craft micro-inductors rooted in commercial $Fe_{73.5}Si_{13.5}B_9Nb_3Cu_1$ (FINEMET) amorphous alloy. Utilizing femtosecond laser processing allows for precise amorphous alloy shaping without inducing crystallization, preserving their intrinsic mechanical excellence. This paper delves into a systematic exploration of both the inductance and flexibility of these fabricated mini-inductors.

2. Results and Discussion

2.1. Preparation of Flexible Mini-Inductors by Femtosecond Laser

Figure 1 shows the schematic illustration for the fabrication process and the optical images of the flexible inductors. As depicted in Figure 1a, the circular spiral inductors are meticulously crafted from an amorphous alloy ribbon utilizing a focused femtosecond laser, exhibiting an impressive beam diameter of ≈10 μm. Subsequently, the inductor is anchored onto a polyimide film using epoxy resin, facilitating the assessment of its electromagnetic properties and inherent flexibility. The miniaturized dimensions of these inductors are notably congruent with fingerprint spacings, as illustrated in Figure 1b. A more detailed optical portrayal of a nine-turn inductor coil, measuring 2 mm in diameter, is presented in Figure 1c. This coil boasts a uniform inter-line spacing of around 10 μm, while the coil line measures 70 μm in width and 18 μm in thickness. Evidently, the femtosecond laser exhibits exceptional machining precision, aptly fulfilling the exacting standards of micro-device fabrication.

Moreover, the amorphous alloy-derived inductor demonstrates exceptional flexibility and elasticity. Figure 1d presents a bending assay of the inductor, while Figure 1e–g elucidate its superior elasticity, evidencing its capacity to stretch by 5 mm when manipulated with tweezers.

2.2. Morphology and Microstructure of Flexible Coils

The micromorphology of the inductance coil after ablation with different laser parameters is shown in Figures S1 and S2 (Supporting Information). The faster processing speed will make the ablation incomplete. We also characterize the roughness of the ablated edges at different powers, as shown in the Figure S3 (Supporting Information). A larger surface roughness usually deteriorates the soft magnetism by pinning the motion of magnetic domain walls. Operating at 300 mW required less energy compared to 400 mW, aligning with our endeavor to develop a process that is not only effective but also energy-efficient.

As shown in Figure S4 (Supporting Information), the XRD pattern of the mini-inductor looks like completely amorphous. No obvious crystalline diffraction peaks are detected. To delve into the microstructural attributes of the ablation zone, we utilized Transmission Electron Microscopy (TEM) for

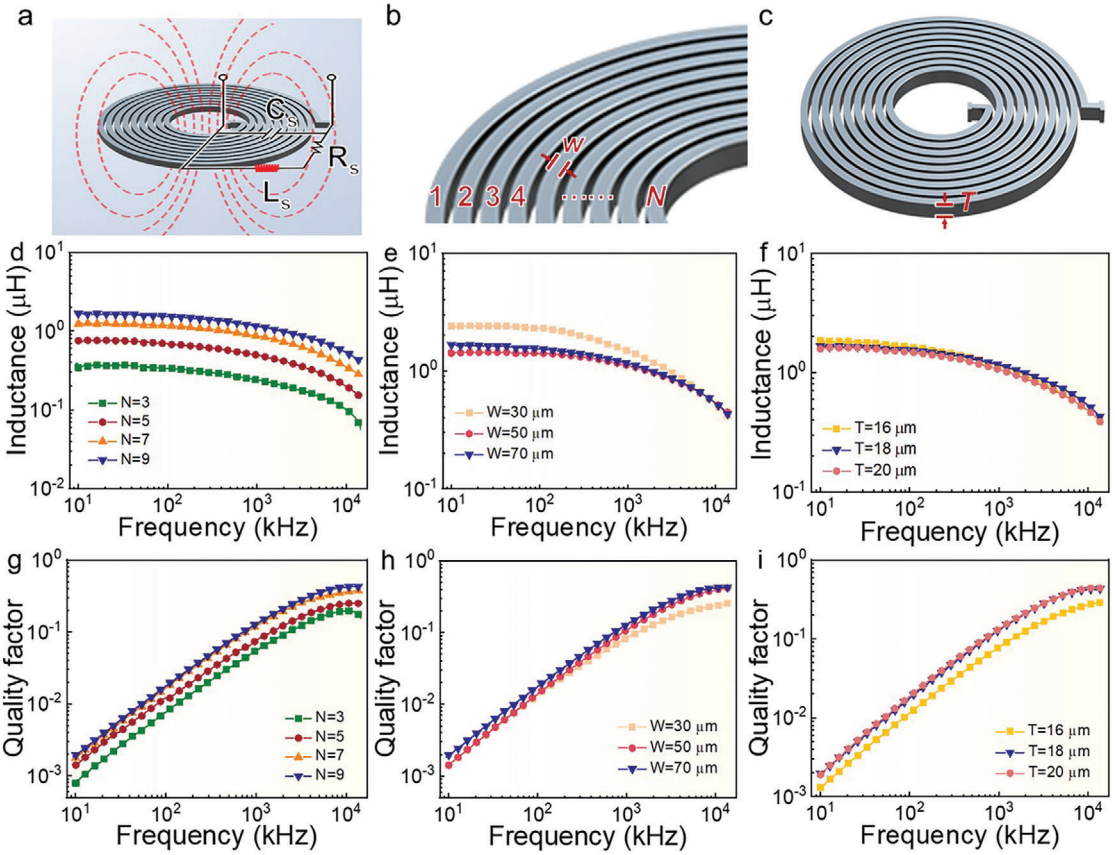

Figure 2. a) Schematic illustration of a spiral inductor and its equivalent circuit (two-port network). b) The top view of the spiral inductor with *N* turns and the width (*W*) of the coil wire. c) The side view of the spiral inductor with thickness of (*T*). Impacts of layout parameters of d) & g) *N*, e) & h) *W*, and f) & i) *T* on the flexible inductors' performance of inductance and quality factor.

characterization. Upon analysis at 300 mW laser power, as shown in Figure S5 (Supporting Information), we observed a minimal thermal effect, with the heat-affected zone spanning a mere 300 nm. This indicates a limited thermal influence during the femtosecond laser processing, validating our choice of laser parameters.

Figure S6 (Supporting Information) shows the performance of inductors under different laser processing parameters, and it can be seen that the power has little effect on the performance of inductors. However, the inductance value and quality factor of the inductor with the machining speed of 1 mm s^{-1} are reduced (Figure S6c,d, Supporting Information), which can be understood from the micromorphology due to the excessive speed and incomplete ablation and the interconnection between the coils. By analyzing the performance of the flexible inductor and the micromorphology of the ablation zone, the optimal laser processing parameters were determined as following: the repetition rate (*f*) is 100 kHz, the laser power (*P*) is 300 mW, and the machining speed (*v*) is 0.5 mm s^{-1}.

2.3. Performance of Flexible Mini-Inductors

The frequency-dependent electromagnetic properties of the flexible spiral inductor are measured using impedance analyzer. The inductance is calculated based on a classical circuit as shown in **Figure 2**a, where R_s is the DC resistance, the L_s is the inductance and C_s is the inherent capacitance of the inductor. The quality factor of an inductor can be expressed as $Q = \omega L/R$,[29] here, ω is angular frequency, *L* stands for the total inductance, and *R* accounts for the metal resistance. Here we change the number of coil turns (*N*), the width (*W*) and thickness (*T*) of the wire to study their influences on the inductance, which is illustrated in Figure 2b-c. The impact of *N* on the performance of the planar inductor is shown in Figure 2d,g. As *N* increases, the inductance and the quality factor of the inductor increase, which can be explained by the following equation:[30]

$$L = 0.002l\{\ln[2l/(W+T)] + 0.25049 + [(W+T)/3l] + \mu/4\} \quad (1)$$

where *L* is inductance in nH; *l* is wire length in cm; *W* is width in cm; *T* is thickness in cm; μ is the permeability. Because the inner diameter of the inductor is fixed, the length of the inductor coil will increase with the number of turns *N*, and then both the self-inductance and mutual inductance increase along with *N*. The measured inductance value at 1 MHz are 240, 491, 865, and 1155 nH for $N = 3$, 5, 7, and 9. Even though the resistance R_s increase along with the length of inductor coil, the quality factor increases with the number of coil turns.

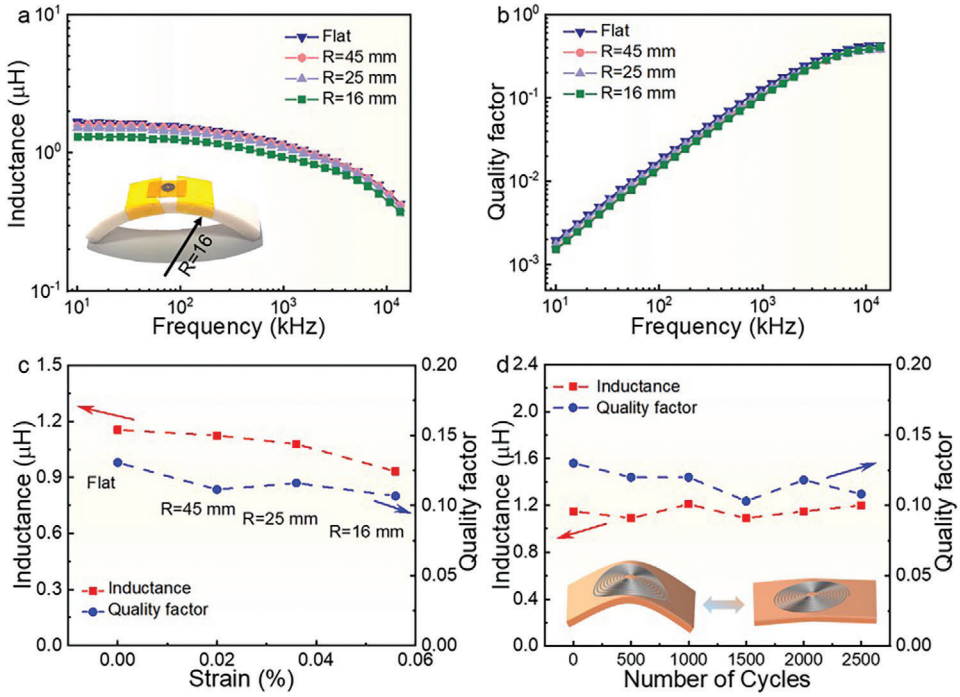

Figure 3. Frequency dependences of a) inductance (The inset diagram shows the inductor at a bend radius of 16 mm) and b) quality factor for the amorphous flexible inductor under flat and bending conditions. Measured inductance and quality factor at 1 MHz of the amorphous flexible inductor c) under different bending radii and d) after the bending cycles (up to 2500 cycles) (Inset picture for the inductor's cyclic bending diagram).

The influence of the coil width on the performance of the planar inductor is shown in the Figure 2e,h. With the increase in the coil width, the effective inductance value of the inductor decreases but the quality factor increases. The decrease in inductance can be attributed to the decrease in mutual inductance between the conducting wires. Large W increases the cross-sectional area of the conductor wires, and hence reduces the ohmic loss and eventually leads to the increase of the quality factor.

The effect of the coil thickness T on the inductor is shown in Figure 2f,i. With the increase of the coil thickness from 16 to 20 μm, the inductance does not change very much but the quality factor increases. The influence of the coil thickness T on quality factor should be similar with the coil width W. Both affect the

Table 1. Comparison of the performance of 2D micro-inductors.

Serial number	Magnetic material	Frequency [MHz]	Inductance [nH]	Inductor size [mm^2]	Inductance density [nH mm^{-2}]	Refs.
1	none	30 000	1.8	0.04	45	[34]
2	none	4	128	1.03	124	[35]
3	$Ni_{45}Fe_{55}$	20	204	2.9	70.3	[36]
4	$Ni_{45}Fe_{55}$	5.5	440	11.52	38.2	[37]
5	FeHfN	5	296	25	11.8	[38]
6	FeTaN	5	1100	78	14.1	[39]
7	NiZnCuFeO	10	48.5	25	1.9	[40]
8	NiZnCuFeO	1	367	22.7	16.2	[41]
9	NiZn	6	430	9	47.8	[42]
10	CoZrO	8.3	1193	50	23.9	[43]
11	Amorphous (FeSiBNbCu)	1	1155	3.14	368	This work
12	Amorphous (FeSiBNbCu)		865	2.22	390	This work
13	Amorphous (FeSiBNbCu)		491	1.45	338	This work
14	Amorphous (FeSiBNbCu)		240	0.85	282	This work

inductor by changing the cross section of the conductor, thereby changing its current density and ohmic loss. But the change in thickness does not influence on the mutual inductance between coil wires, which should account for the little change in inductance.

We have indeed conducted parallel experiments using other soft magnetic amorphous materials, such as the $Fe_{78}Si_9B_{13}$ amorphous alloy, and self-developed $Fe_{82}Si_{3.6}B_{8.4}P_{3.6}Ni_1Mo_{0.4}Cu_1$ amorphous alloy to prepare mini-inductors under the same laser processing conditions for comparison with FINEMET components (Figure S7, Supporting Information). All the mini-inductors show high inductance ranging from 1 μH to 9 μH at 10 kHz, which demonstrates that the laser ablation technique is generally applicable for designing mini-inductors based on different types of amorphous alloys. The relative permeability of the amorphous ribbons of these components are shown in Figure S7d (Supporting Information). As expected, the inductance value is positively correlated with the permeability of the ribbons. It is worthy to note that these alloys have not been annealed to avoid the embrittlement. The non-magnetic materials, such as Cu has also been applied to design mini-inductors. But the inductance for the Cu mini-inductor is limited to below 0.09 μH. Overall, the high permeability of amorphous soft magnetic materials will reduce the magnetic leakage and thus greatly increase the inductance value of the inductor.

For the FINEMET alloy, inducing nanocrystallization through annealing considerably enhances its magnetic properties, with permeability being a standout characteristic. The annealing influence is delineated in Figure S8 (Supporting Information). Evidently, as seen in Figure S8a (Supporting Information), permeability ascends concomitantly with rising annealing temperatures. In concordance, Figure S8b (Supporting Information) captures the inductance values at these varied annealing temperatures, highlighting a direct positive linkage between inductance and permeability. Notably, post-annealing at 993 K, the inductance peaks at 13 μH, demonstrating robust stability across a broad frequency spectrum. A comparison of the quality facto for inductors pre and post annealing is showcased in Figure S8c (Supporting Information). At lower frequencies, the quality factor for nanocrystalline inductors outperforms that of their amorphous counterparts. However, this superiority diminishes as frequencies climb. While Figure S8a,b (Supporting Information) elucidate the augmented permeability and inductance post-annealing, the material's mechanical attributes should not be overlooked. As depicted in Figure S8d (Supporting Information), an annealed crystallized inductor fractures upon bending. This hints at the reduced flexibility associated with crystallized amorphous alloys, primarily attributed to the inception of grain boundaries. Such a compromise in mechanical adaptability upon crystallization is corroborated by prior research, underscoring the challenges in harmonizing magnetic and mechanical properties for flexible applications.[31,32]

To delve into the impact of bending on the attributes of the flexible inductors, we assessed the inductor's performance across varying bending radii. For this assessment, we employed a nine-turn inductor coil with specifications of 2 mm diameter, 70 μm wire width, 10 μm spacing, and 18 μm thickness. **Figure 3**a,b delineate the frequency-dependent variations in inductance value and quality factor for the flexible spiral inductor, contrasting its flat versus bent configurations. Remarkably, both the inductance and the quality factor of this inductor manifest commendable stability across these states. The correlation between the strain borne by the device in its bent state and the associated bending radius can be articulated as follows:[18,33]

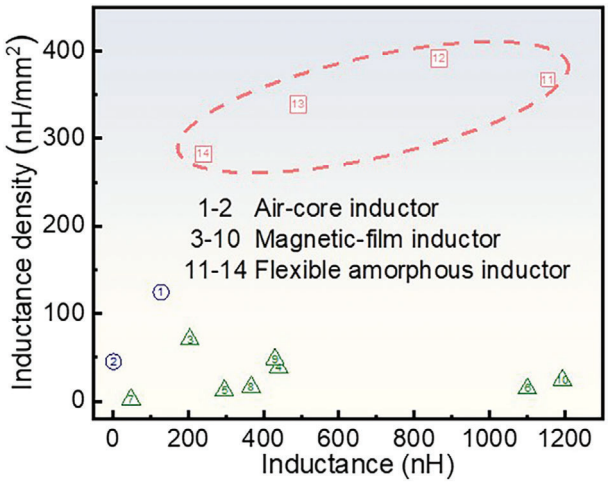

Figure 4. Comparisons in the inductance value and inductance density of this flexible amorphous soft magnetic inductors with literature reported previously air-core inductors and magnetic thin film inductors.

$$\varepsilon = \frac{h}{2R + h} \tag{2}$$

where ε is the maximum strain in bending state, h the thickness of the mini-inductor and R is the radius of bending curvature. Figure 3c delineates the relationship between inductance and quality factor in relation to bending strain. Notably, both parameters exhibit marginal declines, even under a pronounced bending radius of 16 mm, corresponding to a strain (ε) of 0.056%. This resilience underscores the proficient magnetic flux concentration, a testament to the superior magnetic permeability inherent to the amorphous alloys. Further highlighting the inductor's mechanical robustness, Figure 3d showcases the inductor's stability over 2500 bending cycles at a 16 mm bending radius. The inductance and quality factor (evaluated at 1 MHz) of this flexible inductor remain remarkably consistent throughout, indicating its pronounced resistance to bending-induced stresses.

The flexible inductors are compared with the air-core planar inductors [34,35] and typical magnetic thin film inductors such as NiFe,[36,37] FeHfN,[38] FeTaN,[39] NiZnCuFeO,[40,41] NiZn,[42] and CoZrO.[43] **Table 1** enumerates the materials, dimensions, inductance values, and inductance densities of inductors both from existing literature and those fabricated in this study. Concurrently, a comparative analysis of reported inductance values against inductance density is graphically represented in **Figure 4**. A salient observation is that the inductors conceptualized in this work strikingly attain both a significant inductance value and an augmented inductance density, outperforming many counterparts from prior studies.

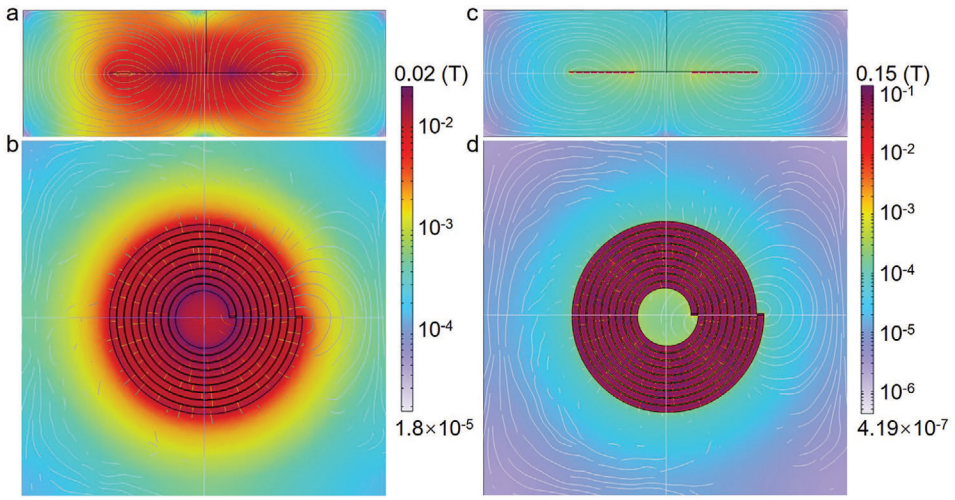

Figure 5. Magnetic flux lines cross-sectional a) & c) and b) & d) surface area of planar spiral coils with Cu a) & b) and soft magnetic amorphous alloys c) & d) as conductors, respectively.

To elucidate the exceptional attributes of the amorphous spiral inductors, a finite element model was employed to simulate the magnetic field distribution within a planar spiral coil's cross-section. This coil, characterized by a width of 70 μm, encompasses 9 turns with a 10 μm inter-trace spacing. **Figure 5** illustrates the magnetic field for two distinct conductors, with a coil excitation of 1 V. As discerned from Figure 5a,b, the magnetic flux density borne by the coil using Cu as the conductor remains relatively subdued (≈10^{-2} T), with the magnetic flux not being confined solely to the coil plane. Notably, pronounced leakage is evident beyond the coil plane, as indicated by the red and yellow zones. Contrastingly, the magnetic field produced by the amorphous soft magnetic wires exceeds that of Cu by an order of magnitude. The flux remains predominantly within the material, with minimal external leakage, as revealed in Figure 5c,d. Consequently, the miniaturized spiral inductors leveraging soft magnetic amorphous alloys manifest unparalleled flexibility and elevated inductance. This observation presents an innovative approach and strategy toward the further miniaturization of electronic components. The inductors also have good bias properties in external field. As we can see in the Figure S9 (Supporting Information), the inductance keeps almost unchanged up to 10 Oe. This suggests a good bias-tolerance property.

2.4. Demonstration of DC-DC Converter with the Flexible Mini-Inductor

We integrate the inductor into the DC/DC circuit to better demonstrate its excellent electrical performance and flexibility. **Figure 6a** presents the circuit schematic and the measurement configuration employed to assess the performance of the flexible mini-inductor. This crafted mini-inductor was integrated onto a commercially sourced LM2576-3.3BT buck converter evaluation board, which operates at a frequency of 52 kHz. With an input voltage spectrum spanning 4 to 40 V (a 5 V input was selected for this study), the board delivers an adjustable output voltage scaled down to 3.3 V. As can be seen in Figure S10 (Supporting Information), the output voltage is stable at 3.3 V over a wide range of input voltages. Given the miniaturized footprint of the inductor, to safeguard circuit functionality and measurement precision, a probe was utilized as a connector bridging the inductor and the circuit board. As evidenced in Figure 6b,c, the flexible mini-inductor sustains operational integrity in both flat and bent conformations. The resultant output voltage closely aligns with the anticipated 3.3 V, achieving an efficiency approximately ≈70%. This shows that the flexible inductor has good stability.

3. Conclusions

In this study, we introduce a novel approach to crafting high energy density, flexible miniature inductors. These spiral inductors are meticulously sculpted from amorphous alloy ribbons using a high-precision focused femtosecond laser. Adopting amorphous soft magnetic materials directly as conductors substantially mitigates magnetic flux leakage, augmenting both the inductance and energy density due to their elevated magnetic permeability. For the diminutive (sub-millimeter) inductors fabricated from $Fe_{73.5}Si_{13.5}B_9Nb_3Cu_1$ amorphous alloy, they achieved an impressive inductance of 1.15 μH at 1 MHz, with an inductance density standing at 368 nH mm^{-2}. Appropriate annealing further escalates this inductance by ≈3–10 times. Moreover, these amorphous alloy-based inductors exhibit stellar mechanical attributes, showcasing exceptional bendability. Even after enduring 2500 bending cycles, the inductor's performance remained intact. Successfully integrating this flexible mini-inductor into a buck-converter evaluation board, we observed a consistent output voltage (steady at 3.3 V) and achieved a zenith efficiency close to 70% at 52 kHz. These findings illuminate pathways to fabricate inductors with heightened inductance density for flexible electronics, providing flexibility in tailoring inductor geometries to meet specific circuitry demands.

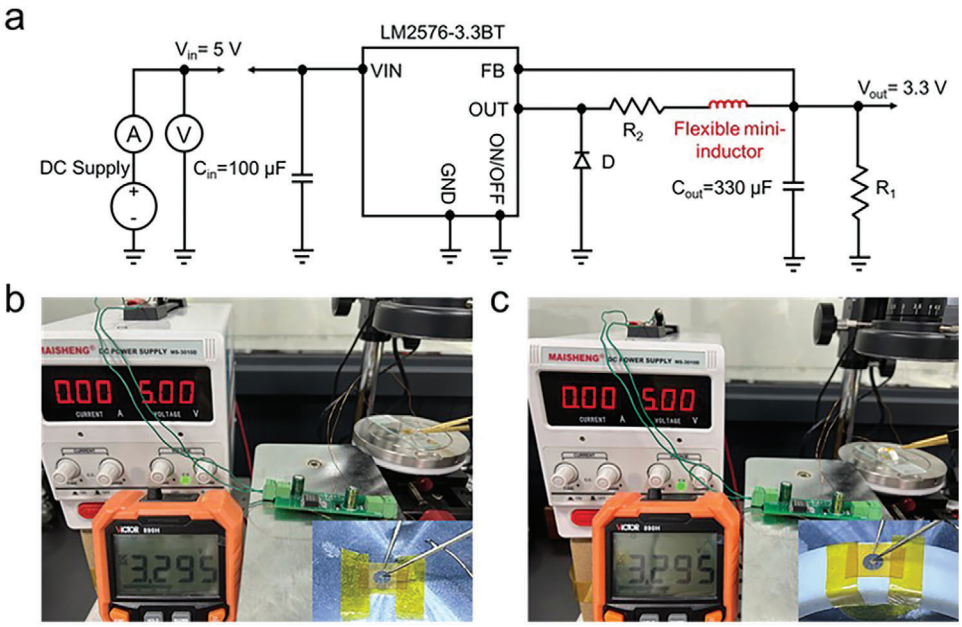

Figure 6. a) Demo circuit of the inductor and the measurement system. b) and c) are the pictures of the normal operation of the flexible inductor in the flat state and the bending state, respectively.

4. Experimental Section

Characterization of the Amorphous Ribbons: In this study, the $Fe_{73.5}Si_{13.5}B_9Nb_3Cu_1$ (at.%) amorphous alloy ribbons was prepared by a single roller melt spinner with high-purity raw materials (>99.95 wt.%). The thickness of the ribbons is about 20 μm and the width is ≈5 mm. The amorphous nature for the ribbon samples of can be verified by X-ray diffraction (XRD, Bruker D8 Advance) and differential scanning calorimetry (DSC, 404 C, Germany). The XRD curve for the $Fe_{73.5}Si_{13.5}B_9Nb_3Cu_1$ ribbon exhibits a broad halo peak at 2θ angles ≈44.5°, which suggests the amorphous nature of the Fe-based ribbons (Figure S11, Supporting Information). The DSC curve is composed of two exothermic crystallization peaks, with the first peak at ≈796 K (inset Figure S11, Supporting Information). The coefficient of thermal expansion (CTE) for the $Fe_{73.5}Si_{13.5}B_9Nb_3Cu_1$ amorphous alloys at different temperatures was measured at a heating rate of 5 K min^{-1} using a TMA 402F3 (Netzsch) for constant flow of a high purity helium gas. The thermal expansion is very small and has negligible effect to result in mechanical distortions (Figure S12, Supporting Information). The permeability of amorphous was measured by an impedance analyzer (Agilent 4294A) from 1 kHz to 10 MHz with the solenoid in two-terminal-connection configuration.

Design and Fabrication of Flexible Mini-Inductors: A fiber laser (Femto YL-Green) with a wavelength of 515 nm and a beam diameter of about 10 μm was employed to ablate the amorphous ribbons into inductor coils. To facilitate the characterization of the flexibility of the inductors, epoxy film was used as adhesive (at 398 K) to combine the flexible micro amorphous inductors prepared by laser micro-nano technology with flexible substrate polyimide. In order to obtain the inductor coil with high precision and uniform ablation zone, the influence of the laser parameters was studied.

Testing of Flexible Mini-Inductors: The impedance frequency characteristics were measured by a Wayne Kerr 1J6515 impedance measuring equipment with two probes. The diameter of the probe tip is ≈10 μm. The series circuit is chosen as the equivalent circuit for measuring the inductance value. The connection of the probe to the impedance analyzer is achieved through a Wayne Kerr two-wire to four-wire connection to ensure accurate measurement of inductance. Test photos and connection cables are shown in Figure S13 (Supporting Information). The equivalent circuit analysis of an inductor can be reduced to a simple RLC circuit model, which is equivalent to a series equivalent circuit here. The impedance measurements (Bode plot), as shown in the Figure S14 (Supporting Information). The phase angle increases along with increasing the frequency. Until 10 MHz, the phase angle doesn't reach a maximum, which means that the inductor can work at a much higher frequency. Cyclic bending experiment was conducted at ambient temperature using a universal material mechanics testing machine (Zwick/Roell Z1.0). The picture and video of the inductor during the cyclic bending process is shown in Figure S15 (Supporting Information).

Morphology and Structure Characterization of Flexible Mini-Inductors: The morphology of the laser ablation samples was characterized by an optical microscope and scanning electron microscope (SEM, Hitachi, S4800). The surface roughness of the samples was characterized by a scanning probe microscope (SPM, Dimension 3100) and the characterization area was 5 μm × 5 μm. High-resolution characterizations of microstructure at the laser ablation edge were performed by focused ion beam (FIB, Zeiss Auriga) and a transmission electron microscope (TEM, Talos F200x).

Supporting Information

Supporting Information is available from the Wiley Online Library or from the author.

Acknowledgements

Y.C., J.W., and Y.Z. contributed equally to this work. Financial support was provided by the "Pioneer and Leading Goose" R&D Program of Zhejiang (2022C01023), National Natural Science Foundation of China (NSFC 52231006, 52101205, 92163108, 51922102), Special Foundation of Director of Ningbo Institute of Materials Technology & Engineering (E30101QF01, Grant No.2021SZKY0309), and Science and Technology Service Network Initiative (2022T3038).

Conflict of Interest

The authors declare no conflict of interest.

Data Availability Statement

The data that support the findings of this study are available in the supplementary material of this article.

Keywords

excellent bendability, femtosecond laser ablation, flexible mini-inductors, high inductance density, soft magnetic amorphous alloys

Received: October 27, 2023
Revised: January 23, 2024
Published online:

[1] R. H. Reuss, B. R. Chalamala, A. Moussessian, M. G. Kane, A. Kumar, D. C. Zhang, J. A. Rogers, M. Hatalis, D. Temple, G. Moddel, B. J. Eliasson, M. J. Estes, J. Kunze, E. S. Handy, E. S. Harmon, D. B. Salzman, J. M. Woodall, M. A. Alam, J. Y. Murthy, S. C. Jacobsen, M. Olivier, D. Markus, P. M. Campbell, E. Snow, *Proceedings of the IEEE* **2005**, *93*, 1239.
[2] Z. Shi, L. Meng, X. Shi, H. Li, J. Zhang, Q. Sun, X. Liu, J. Chen, S. Liu, *Nano-Micro Lett.* **2022**, *14*, 141.
[3] Y. Khan, A. Thielens, S. Muin, J. Ting, C. Baumbauer, A. C. Arias, *Adv. Mater.* **2020**, *32*, 1905279.
[4] P. Wang, M. Hu, H. Wang, Z. Chen, Y. Feng, J. Wang, W. Ling, Y. Huang, *Adv. Sci. (Weinh)* **2020**, *7*, 2001116.
[5] L. Li, Z. Wu, S. Yuan, X.-B. Zhang, *Energy Environ. Sci.* **2014**, *7*, 2101.
[6] S. R. Forrest, *Nature* **2004**, *428*, 911.
[7] Y. Sun, J. A. Rogers, *Adv. Mater.* **2007**, *19*, 1897.
[8] S. Nabavi, S. Bhadra, *IEEE Sens. J.* **2022**, *22*, 1980.
[9] N. Wang, T. O'Donnell, S. Roy, M. Brunet, P. McCloskey, S. C. O'Mathuna, *J. Magn. Magn. Mater.* **2005**, *290-291*, 1347.
[10] X.-L. Tang, H. W. Zhang, H. Su, Y. Shi, X. D. Jiang, *J. Magn. Magn. Mater.* **2005**, *294*, 49.
[11] D. Mishra, P. M. Raj, R. Tummala, *Microelectron. Eng.* **2016**, *160*, 34.
[12] M. Chen, G. Ding, P. Cheng, C. Zhang, X. Zhu, Z. Liu, *Micromachines* **2017**, *8*, 151.
[13] D. Mishra, P. M. Raj, J. Tishler, T. Sun, E. Shipton, R. Tummala, *IEEE Trans. Magn.* **2016**, *52*, 2800905.
[14] H. Wu, M. Khdour, P. Apsangi, H. Yu, *IEEE Trans. Magn.* **2017**, *53*, 2004507.
[15] M. Woytasik, J. P. Grandchamp, E. Dufour-Gergam, E. Martincic, J. P. Gilles, S. Megherbi, V. Lavalley, V. Mathet, *Microsystem Technologies* **2006**, *12*, 973.
[16] L. Sun, G. Qin, H. Huang, H. Zhou, N. Behdad, W. Zhou, Z. Ma, *Appl. Phys. Lett.* **2010**, *96*, 013509.
[17] W. J. Freitas, M. H. O. Piazzetta, L. T. Manera, Â. L. Gobbi, *Journal of Vacuum Science & Technology B* **2020**, *38*, 023204.
[18] M. Bissannagari, W. Lee, W. Y. Lee, J. H. Jeong, J. Kim, *Adv. Funct. Mater.* **2017**, *27*, 1701766.
[19] H. Wang, M. Totaro, S. Veerapandian, M. Ilyas, M. Kong, U. Jeong, L. Beccai, *Adv. Mater. Technol.* **2020**, *5*, 2000659.
[20] K. S. M. Yamaguchi, Y. Takahashi, K. I. Arai, S. Kikuchi, Y. Shimada, S. Tanabe, K. Ito, *J. Magn. Magn. Mater.* **2000**, *215*, 807.
[21] Y. Chen, L. Feng, R. Tian-Ling, L. Li-Tian, C. Guang, G. Xiao-Kang, A. Wang, F. Hai-Gang, *IEEE Electron Device Lett.* **2007**, *28*, 652.
[22] R. S. Yang, A. J. Hanson, B. A. Reese, C. R. Sullivan, D. J. Perreault, *IEEE Trans. Power Electron.* **2019**, *34*, 9993.
[23] G. Herzer, *Acta Mater.* **2013**, *61*, 718.
[24] W.-H. Lin, C.-M. She, C.-Y. Zhang, P. S. Branicio, Z.-D. Sha, *International Journal of Plasticity* **2022**, *156*, 103373.
[25] C. Xie, W. Li, F. Shen, Y. Liu, L. Xie, Z. Liao, S. Zhong, *J. Non-Cryst. Solids* **2018**, *499*, 58.
[26] F. L. Kong, C. T. Chang, A. Inoue, E. Shalaan, F. Al-Marzouki, *J. Alloys Compd.* **2014**, *615*, 163.
[27] M. Sorescu, T. Xu, S. Herchko, *J. Magn. Magn. Mater.* **2011**, *323*, 2859.
[28] X. Li, J. Zhou, L. Shen, B. Sun, H. Bai, W. Wang, *Adv. Mater.* **2023**, *35*, 2205863.
[29] E. Gamet, J. P. Chatelon, T. Rouiller, B. Bayard, G. Noyel, J. J. Rousseau, *J. Magn. Magn. Mater.* **2005**, *288*, 121.
[30] X.-L. Li, G.-Z. Chai, D.-W. Guo, B. Gao, Z.-M. Zhang, D.-S. Xue, *Microelectron. Eng.* **2009**, *86*, 2290.
[31] J. Schroers, W. L. Johnson, *Phys. Rev. Lett.* **2004**, *93*, 255506.
[32] P. Vahdati Yekta, A. Ghasemi, E. M. Sharifi, *J. Magn. Magn. Mater.* **2018**, *468*, 155.
[33] G. Qin, H.-C. Yuan, G. K. Celler, J. Ma, Z. Ma, *Appl. Phys. Lett.* **2010**, *97*, 233110.
[34] J. Kang, Y. Matsumoto, X. Li, J. Jiang, X. Xie, K. Kawamoto, M. Kenmoku, J. H. Chu, W. Liu, J. Mao, K. Ueno, K. Banerjee, *Nat. Electron.* **2018**, *1*, 46.
[35] C. D. Meyer, S. S. Bedair, B. C. Morgan, D. P. Arnold, *IEEE Trans. Power Electron.* **2014**, *29*, 6052.
[36] S. Peng, J. Yu, C. Feeney, T. Ye, Z. Zhang, N. Wang, *J. Magn. Magn. Mater.* **2021**, *524*, 167661.
[37] W. Ningning, T. O'Donnell, R. Meere, F. M. F. Rhen, S. Roy, S. C. O'Mathuna, *IEEE Trans. Magn.* **2008**, *44*, 4096.
[38] Y.-M. Kuo, J.-G. Duh, *J. Magn. Magn. Mater.* **2012**, *324*, 1084.
[39] C.-S. K. Dong-Hoon Shin, J.-H. Jeong, S.-E. Nam, H.-J. Kim, *IEEE Transactions on Maonbtics* **1999**, *35*, 3511.
[40] B. Seok, H. Yang-Ki, L. Jae-Jin, J. Jalli, G. S. Abo, A. Lyle, B. C. Choi, G. W. Donohoe, *IEEE Trans. Magn.* **2009**, *45*, 4773.
[41] R. Anthony, N. Wang, D. P. Casey, C. Ó Mathúna, J. F. Rohan, *J. Magn. Magn. Mater.* **2016**, *406*, 89.
[42] J. Li, V. F.-G. Tseng, Z. Xiao, H. Xie, *IEEE Trans. Power Electron.* **2017**, *32*, 3858.
[43] D. V. Harburg, A. J. Hanson, J. Qiu, B. A. Reese, J. D. Ranson, D. M. Otten, C. G. Levey, C. R. Sullivan, *IEEE Journal of Emerging and Selected Topics in Power Electronics* **2018**, *6*, 1280.

